nature biotechnology

Multiplexed precision genome editing with trackable genomic barcodes in yeast

Kevin R Roy[1–4,11], Justin D Smith[1,4,11], Sibylle C Vonesch[5,11], Gen Lin[5], Chelsea Szu Tu[5], Alex R Lederer[5], Angela Chu[1,6], Sundari Suresh[1,6], Michelle Nguyen[1,4], Joe Horecka[1,6], Ashutosh Tripathi[7], Wallace T Burnett[1,4], Maddison A Morgan[1,4], Julia Schulz[1,4], Kevin M Orsley[1,4], Wu Wei[1,4], Raeka S Aiyar[1], Ronald W Davis[1,4,6], Vytas A Bankaitis[7–9], James E Haber[10], Marc L Salit[2,3], Robert P St.Onge[1,6] & Lars M Steinmetz[1,3–5]

Our understanding of how genotype controls phenotype is limited by the scale at which we can precisely alter the genome and assess the phenotypic consequences of each perturbation. Here we describe a CRISPR–Cas9-based method for multiplexed accurate genome editing with short, trackable, integrated cellular barcodes (MAGESTIC) in *Saccharomyces cerevisiae*. MAGESTIC uses array-synthesized guide–donor oligos for plasmid-based high-throughput editing and features genomic barcode integration to prevent plasmid barcode loss and to enable robust phenotyping. We demonstrate that editing efficiency can be increased more than fivefold by recruiting donor DNA to the site of breaks using the LexA–Fkh1p fusion protein. We performed saturation editing of the essential gene *SEC14* and identified amino acids critical for chemical inhibition of lipid signaling. We also constructed thousands of natural genetic variants, characterized guide mismatch tolerance at the genome scale, and ascertained that cryptic Pol III termination elements substantially reduce guide efficacy. MAGESTIC will be broadly useful to uncover the genetic basis of phenotypes in yeast.

Predicting the functional consequences of genetic variation is one of the fundamental challenges in understanding phenotypic diversity, engineering desirable traits for biotechnology, and enabling precision medicine. Although CRISPR screens have been used extensively to disrupt function through the introduction of non-homologous end-joining (NHEJ)-mediated small insertions/deletions (indels) and premature termination codons (PTCs) in open reading frames (ORFs), few methods have been developed to introduce specific amino acid and nucleotide variants at the genome scale.

High-throughput approaches for genome editing have been described in prokaryotes[1] and more recently in yeast[2,3], but these studies have not explored natural genetic variation. Here we describe a CRISPR–Cas9-based method in *S. cerevisiae* for multiplexed genome editing, with array-synthesized guide RNA/donor DNA (guide–donor) oligonucleotides, that overcomes major shortcomings in currently employed approaches. First, we introduce stable, genome-integrated barcodes instead of plasmid barcodes, thereby enabling marker-free variant tracking and one-to-one correspondence of barcode counts to strain abundance. Second, we demonstrate a more than fivefold increase in precision editing efficiency by active recruitment of donor DNA to Cas9-induced double-strand breaks. This improvement enabled saturating a region of the *SEC14* gene with all possible amino acid changes to identify residues modulating sensitivity to the NPPM (nitrophenyl(4-(2-methoxyphenyl) piperazin-1-yl)methanone) class of inhibitors of Sec14p-like phosphatidylinositol transfer protein, attractive drug targets in pathogenic fungi. Finally, we use MAGESTIC to introduce thousands of single-nucleotide polymorphisms (SNPs) and small indels, representing natural variants from the vineyard isolate RM11, into the laboratory strain S288c. We demonstrate the ability to make single-nucleotide variants without requiring protospacer adjacent motif (PAM) mutations, reveal distinct mismatch tolerance between the 19th and 20th positions from the PAM, and ascertain that the presence of cryptic Pol III termination signals in the form of imperfect T-homopolymer stretches is a key factor predicting guide efficiency.

The MAGESTIC workflow

MAGESTIC utilizes pools of array-synthesized oligos encoding a guide RNA, a Type IIS restriction site, and a donor DNA to introduce the designed variant by homologous recombination (**Fig. 1a**). The

guide–donor pairs enable multiplexed engineering of specific genetic variants at desired locations throughout the genome and quantification of variant abundance by sequencing. Synthesis errors in the guide sequence can prevent target recognition and cleavage, and errors in the donor DNA can lead to incorporation of the wrong variant. To enable accurate phenotyping, free from confounding sequencing errors, we tagged each guide–donor pair with a short, unique 31-mer barcode during subpool amplification. Paired-end sequencing assigns each barcode to its corresponding guide–donor sequence and enables full-length sequence verification (**Fig. 1a**). Multiple distinct barcodes mapping to the same guide–donor combination offer the further advantage of internal replicates for a given edit, and can be leveraged as single-cell barcodes[4]. The structural component of the Cas9 guide as well as bacterial- and yeast-specific selectable markers are added via the Type IIS-site in a second cloning step (**Fig. 1b**). Selecting for these markers in step 2 cloning removes uncut step 1 products and ensures a high-quality library, which is then transformed into a population of yeast cells harboring Cas9 (ref. 5).

To enable one-to-one barcode-to-cell correspondence and to eliminate the need for plasmid maintenance, the guide–donor cassette is linearized and integrated into the genome using a dedicated guide (guide X), targeting both the plasmid and a chromosomal barcode locus; insertion is mediated by identical homologies flanking the guide–donor on the plasmid and barcode locus (**Fig. 1b**). The abundance of each variant is assessed after competitive growth in different conditions by next-generation sequencing (NGS) of the 31-mer barcodes, enabling high-throughput profiling of variant function (**Fig. 1c**). To test whether library diversity and uniformity are maintained throughout each step of the pipeline, we cloned a guide–donor library harboring 10^5 members, achieving 2×10^6 distinct barcodes (~20-fold library coverage) in the first step of cloning. Of the 10^5 designed guide–donors, we identified 99% and 94% after the first and second cloning steps, respectively, and 89% after yeast transformation without substantial increase in bias (**Supplementary Fig. 1**).

Simultaneous editing, barcoding, and plasmid destruction

As a proof of principle, we designed a guide–donor plasmid to introduce a PTC into the *ADE2* ORF (*YOR128C*). Disruption of *ADE2* results in accumulation of red pigment, enabling direct visual identification of edited colonies[6]. First we tested three different Pol III promoters (*RPR1*, *SNR52*, and tRNA-Tyr(*SUP4*)-HDV) to drive expression of guide X, and found similar kinetics of barcode integration upon Cas9 induction (**Supplementary Fig. 2**). To assess editing kinetics with MAGESTIC, we quantified the fraction of NHEJ indel and homologous recombination donor repair events in the population by NGS of the *ADE2* locus throughout 15 generations of editing (**Fig. 2a**). Over 9 generations, perfect donor repair events approached 70% with the remaining 30% constituting NHEJ indels (**Fig. 2a**). Precision donor editing rose to nearly 100% in cells lacking the *NEJ1* (*YLR265C*) gene required for efficient NHEJ, corroborating previous reports[2]. Progressive barcode integration reached near-completion by 11 generations as shown by both PCR amplification (**Fig. 2b**) and survival on 5-fluorocytosine, indicating removal of the *FCY1* counter-selectable marker at the barcode locus (**Fig. 2c**). We observed similar kinetics of barcode integration and guide–donor plasmid self-destruction with a complex pool of guide–donors designed to introduce natural variants (**Fig. 2b**). Collectively, these results show that precision editing, genomic barcode integration, and guide–donor plasmid self-destruction all reach near-completion by 9 to 11 generations.
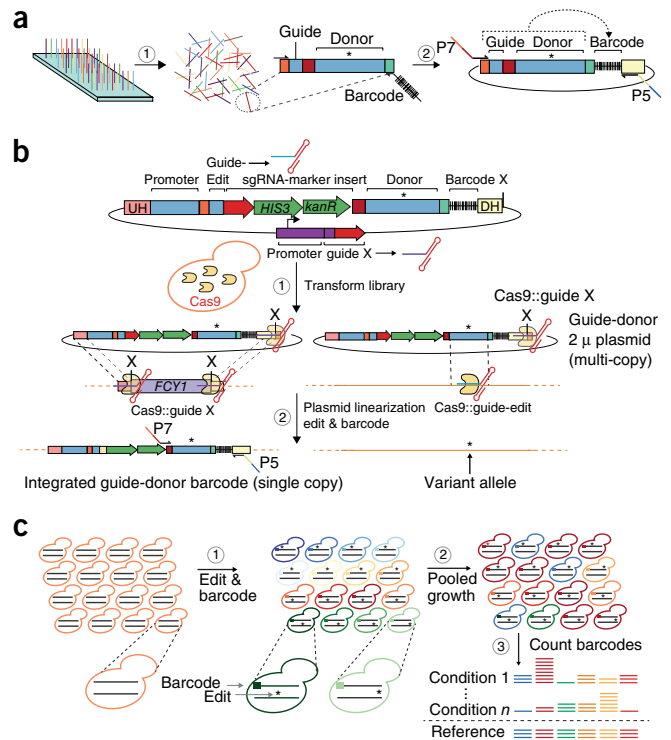
Figure 1 The MAGESTIC pipeline for multiplexed precision genome editing. (**a**) Linking guide–donors to short DNA barcodes. (1) A complex pool of array-synthesized oligonucleotides encoding guide–donors is amplified and cloned to generate the step 1 library. The reverse primer introduces a semi-random 31-mer barcode into each ligation product, and (2) NGS enables sequence validation and computational mapping of each guide–donor sequence in the step 1 library to a unique barcode. (**b**) Insertion of the Cas9 structural guide component plus selection markers from yeast (*HIS3*) and bacteria (*kanR*) in between the guide and donor. (1) This final step 2 library is transformed into yeast cells such that the vast majority of transformants uptake a single plasmid, which accumulates to a high-copy number. Each cell harbors a barcode integration locus with a counter-selectable marker (*FCY1*). Guide-donor plasmids harbor a second guide expression unit (guide X) to promote barcode integration, as guide X cleavage sites flank *FCY1*. (2) Cas9 and guide expression results in simultaneous cleavage of the guide–donor plasmid at a guide X site adjacent to the downstream homology (DH), target site editing (right), and genomic integration of the guide-marker-donor-barcode cassette (left). (**c**) Library-scale genome editing and competitive growth phenotyping. (1) The guide–donor plasmids allow editing throughout the genome, while the barcode integration site is constant. (2) Pooled growth in different conditions results in enrichment or depletion of variants that affect fitness. (3) Variant fold-changes are calculated based on barcode sequencing counts in treated vs. untreated conditions.

Active donor recruitment to breaks improves homologous recombination efficiency

Efficient homologous recombination is particularly important for multiplexed editing as typical array-synthesis error rates of 1 in 200 mean that 10% of guides should harbor at least one error, impairing target cleavage. Furthermore, guides exhibit variable cleavage efficiencies dependent on intrinsic features of the guide sequence and the target DNA locus[7,8]. Because cells with functional guide RNAs will undergo cell-cycle arrest during repair, or will not survive editing and undergo cell death[5,9], cells containing mutated or low efficacy guides will dominate the population.

We hypothesized that homologous recombination efficiency might be limiting for cell survival and sought to enhance efficiency by active recruitment of the donor to double-stranded DNA (dsDNA) breaks. We adapted an endogenous mechanism required for yeast mating type switching from *MAT***a** to *MAT*α[10], where a sequence element called the recombination enhancer (RE) near the *HML*α donor mediates enhanced homologous recombination at the *MAT* locus. *HML*α donor recruitment requires two interactions: the binding of Fkh1p to the RE, and the recruitment of Fkh1p to the *MAT* locus dsDNA break via binding of the forkhead-associated (FHA) domain of Fkh1p to phosphothreonines on multiple proteins[11], including the Mph1p helicase, Fdo1p, and likely additional unidentified proteins[12]. Fusing Fkh1p to the LexA DNA binding domain (LexA–Fkh1p) and replacing the RE with LexA sites partially rescues a deletion of the RE[13]. To adapt this mechanism for MAGESTIC, we introduced a tandem array of four LexA sites on the *ADE2* guide–donor plasmid and introduced LexA–Fkh1p on a plasmid harboring constitutive Cas9 (**Fig. 3a**). We spiked in a plasmid with a nonfunctional guide at 15% to simulate error rates typically observed in oligo libraries. Cells containing a functional *ADE2* guide–donor plasmid, but lacking either LexA–Fkh1p, the LexA sites, or both, were poorly represented, comprising only 8–12% of the surviving colonies (**Fig. 3b** and **Supplementary Table 1**). In contrast, the presence of both LexA–Fkh1p and LexA sites led to a more than fivefold increase in the percentage of edited colonies in both WT and *nej1*Δ backgrounds (**Fig. 3b**), with the fraction of red colonies more closely resembling the plasmid input ratios. NGS of the edited locus from the population confirmed that the increase in red colony fraction occurred through an enhancement of homologous recombination and not NHEJ (**Fig. 3c**), demonstrating that active donor recruitment with the LexA–Fkh1p system specifically increases homologous recombination efficiency.

Saturation editing to dissect a protein–drug interaction

To validate the high-throughput editing capacity of MAGESTIC, we designed a guide–donor library to saturate a region of the essential eukaryotic gene *SEC14* (*YMR079W*) with amino acid substitutions. The Sec14p phosphatidylinositol transfer protein is an attractive drug target in pathogenic fungi[14], and represents the sole essential target of small-molecule inhibitors termed NPPMs[15]. Several mutations that ablate NPPM binding without strongly compromising Sec14p function have been previously identified[15]. As this study employed random mutagenesis to select for NPPM-resistant clones, it likely did not test all possible amino acid substitutions and also was not capable of identifying mutations resulting in increased NPPM sensitivity. We reasoned that saturation mutagenesis could provide a complete map of residues important for Sec14p drug interactions.

High-throughput CRISPR editing requires strategies that prevent donor cleavage by the paired guide, while retaining incorporation of the desired variant. Previous approaches have engineered a synonymous mutation in the PAM in addition to the desired variant[1]. This strategy has limitations because not all PAMs can accommodate synonymous changes, and because the efficiency of incorporating the desired variant is impaired by greater distance from the PAM[1]. Many ORFs also contain regions devoid of NGG SpCas9 PAMs. To circumvent these limitations, we devised a synonymous-codon-spreading strategy that is robust with respect to such 'PAM-deserts' (**Supplementary Fig. 3**). Our strategy involves spreading synonymous mutations from the target codon toward the Cas9 cut site to prevent donor cleavage and ensure incorporation of the entire edit by limiting the length of microhomologous sequence between the Cas9 cleavage site and the target codon. To account for potential effects of
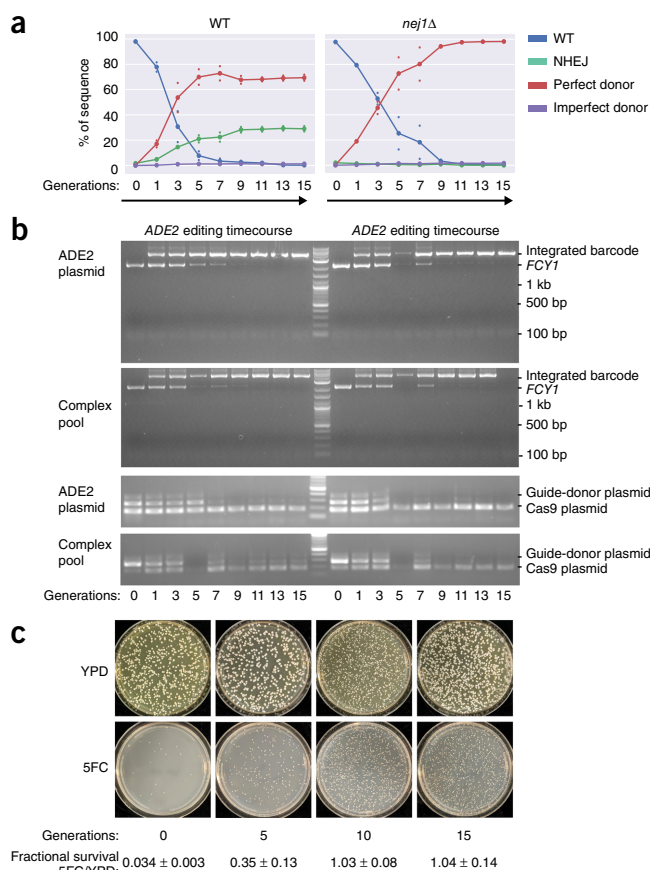

Figure 2 Simultaneous genome editing, guide–donor barcode integration, and plasmid self-destruction. (**a**) WT and *nej1*Δ were transformed with GAL-Cas9 and a guide–donor cassette to introduce a PTC in the *ADE2* gene. Cas9 expression was induced by galactose and aliquots were harvested at the indicated generations. The *ADE2* locus was analyzed by NGS and the fractions of WT sequence, NHEJ indels, and donor-DNA-directed editing (either perfect or imperfect repair) were calculated. The line graph shows the mean percentages at each generation from duplicate experiments. (**b**) Integration of the guide–donor barcode was assayed by amplification targeting the chromosomal barcode locus for the single *ADE2* guide–donor plasmid (top) as well as a complex pool of >100,000 barcoded guide–donor plasmids (bottom). The uncropped gel image indicates an absence of detectable NHEJ indel events at the barcode locus. Self-destruction of the guide–donor plasmids was assessed by a three-primer PCR, with a common forward primer and either a guide–donor plasmid-specific primer (top band) or a Cas9-plasmid-specific primer (bottom band). (**c**) Cultures at the indicated generations of galactose induction were plated in quadruplicate at a density of ~1,000 cells per plate on rich medium (YPD) and *FCY1* counter-selectable medium (5-FC). The fraction of surviving colonies on plates are shown. All experiments were repeated with three biological replicates starting from independent transformations of the guide–donor plasmids. (Full gel images are available in **Supplementary Fig. 9**.)

synonymous changes, we included a synonymous-change-only donor that left the target codon unchanged. In addition, we introduced each target codon twice using upstream and downstream synonymous changes paired with different guides to control for potential off-target effects (**Fig. 4a**).

The mutation of essential genes presents a unique challenge. Each designed mutation that is not detected in the edited pool could either be an unsuccessful edit or a successful, but functionally detrimental,

edit. To resolve these possibilities, we took advantage of previous findings that the lethality of a *SEC14* deletion is suppressed by loss-of-function mutations in *KES1* (*YPL145C*) or *CKI1* (*YLR133W*) that oppose Sec14p-mediated signaling[16–18]. Transforming the guide–donor library into a *KES1*-deficient strain harboring WT *SEC14* enabled recovery of detrimental variants and otherwise lethal PTCs. Mating the edited *SEC14* library to a complementary suppressor strain lacking *CKI1* and *SEC14* but containing *KES1* led to (1) the cellular requirement for *SEC14* function and (2) the sole copy of *SEC14* being the edited variant (**Fig. 4b**). We sequenced the edited window of *SEC14* to assess the counts for each variant, successfully detecting 1,361/1,382 (98.5%) designed variants at the haploid stage. We found <0.5% NHEJ-indel events in the sequenced window, consistent with our results on *ADE2* with cells pre-expressing Cas9 from the constitutive *TEF1* promoter (**Fig. 3c**) as well as previous results[5]. We observed an expected depletion of PTC and proline variants (**Supplementary Fig. 4**), and generated a profile of functionally important residues, including residues highly intolerant to a large number of non-synonymous changes (**Fig. 4c**, top panel).

To identify mutations that rendered Sec14p resistant to NPPM inhibition, we grew the diploid *SEC14* library in the presence or absence of sublethal doses of the NPPM 4130-1276 (ref. 15). This approach revealed a rich profile of mutations conferring both resistance and sensitivity to NPPM (**Fig. 4c**, bottom panel). Replicates of the drug screen revealed high concordance (**Supplementary Fig. 5a**), and results with the upstream and downstream synonymous versions of each edit were similar, indicating that the observed phenotypes were due to coding changes and not the synonymous DNA changes that accompanied them (**Supplementary Fig. 5b**). Our results were also consistent with two previously characterized positions, Y111 and Y122, which frame the Sec14p phosphatidylcholine (PtdCho)-head-group-coordinating substructure[15]. We detected substantial resistance for Y111A and most other Y111 substitutions, with notable exceptions of the Y111Y synonymous control, Y111F, Y111L, Y111I, and Y111M, suggesting that bulky hydrophobic residues at this position stabilize NPPM binding. Previous studies have found that Y122A does not affect sensitivity to NPPMs, while Y122F confers slight resistance[15]. Notably, Y122F and Y122W were the only amino acid changes at position 122 which conferred resistance in our assay. To confirm the accuracy of our high-throughput approach, we chose several specific mutations identified by our screen that, relative to the synonymous controls, increased NPPM resistance (A104D, E124R, L126E/C), decreased resistance (A104C, E124M/F), or showed minimal change (E124G, A104V/Y). Re-creating these mutants without accompanying synonymous changes and phenotyping them individually revealed excellent concordance with the change in drug resistance indicated by our screen (**Fig. 4e** and **Supplementary Table 2**).

Complementing the previously characterized mutations, our approach generated a complete functional map of the Sec14p 102-137 region and its interaction with NPPMs (**Fig. 4c,d**). Functional and mutational hotspots fell under four main categories: (1) positions where most mutations were tolerated for Sec14p function and conferred resistance to NPPM (A104, P108, Y111, H112, D117, and G127); (2) positions where only a few specific amino acid changes conferred resistance, despite most substitutions having no impact on function (e.g., I103D/F/L/W/Y, Q109C/D/G/W, V121F, E125I/V, L126A/C/D/E/V); (3) positions intolerant of most changes, while still permissive for NPPM-resistance mutations (P120F/H/M/S/W, E124R); and (4) positions important for function but harboring no NPPM-resistance alleles (D115, V129). These distinctions are likely the result of a trade-off between preserving the function of the essential
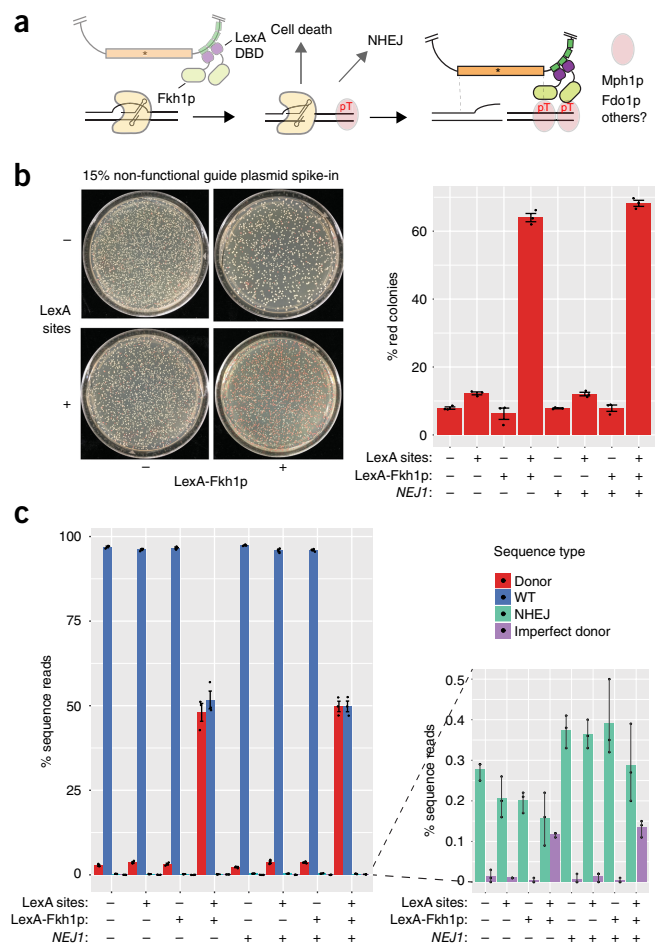

Figure 3 Active recruitment of donor DNA to Cas9-induced dsDNA breaks increases homologous recombination efficiency. (**a**) A protein fusion of Fkh1p to the LexA DNA-binding domain (LexA–Fkh1p) enables recruitment of donor DNA directly to dsDNA breaks (DSBs). DSBs result in the accumulation of proteins phosphorylated on specific threonine residues (pT) near the site of the break. The interaction between Fkh1p and various pT-containing proteins (including Mph1p, Fdo1p, and additional unidentified proteins) recruits LexA–Fkh1p to DSBs, which in turn recruits donor DNA via LexA binding sites on the plasmid. (**b**) *ADE2*-guide donor plasmids with (bottom) or without (top) LexA sites were mixed with a non-functional *ADE2* guide–donor plasmid at a ratio of 17:3, and transformed into a strain pre-expressing TEF1-Cas9 with (right) or without (left) LexA–Fkh1p. Red colonies indicate cells that received a functional *ADE2* guide–donor and survived editing, while white colonies represent cells that received the non-functional *ADE2* guide. The bar chart depicts the mean percentage of red colonies (*y* axis) determined by counting three plates per condition (*x* axis). Error bars represent the s.d. (**c**) The *ADE2* locus was analyzed as in **Figure 2**. Because *ade2* is a detrimental mutation, *ade2* null colonies are smaller and thus contribute slightly fewer sequence reads per colony relative to white colonies. The bar chart (left) indicates that >99.5% of the sequence is WT or perfect donor repair. The inset bar chart (right) shows the remaining <0.5% of editing events (**Supplementary Table 1**).

Sec14p and interfering with binding of an inhibitor, with some residues having a greater impact on one process than the other. NPPM 4130-1276 docking experiments predicted that, while Y111 and P120 face the Sec14p lipid-binding pocket and could directly interfere with NPPM binding, many of the resistance hotspots (e.g., A104, P108, G127) are far removed from the presumptive NPPM binding
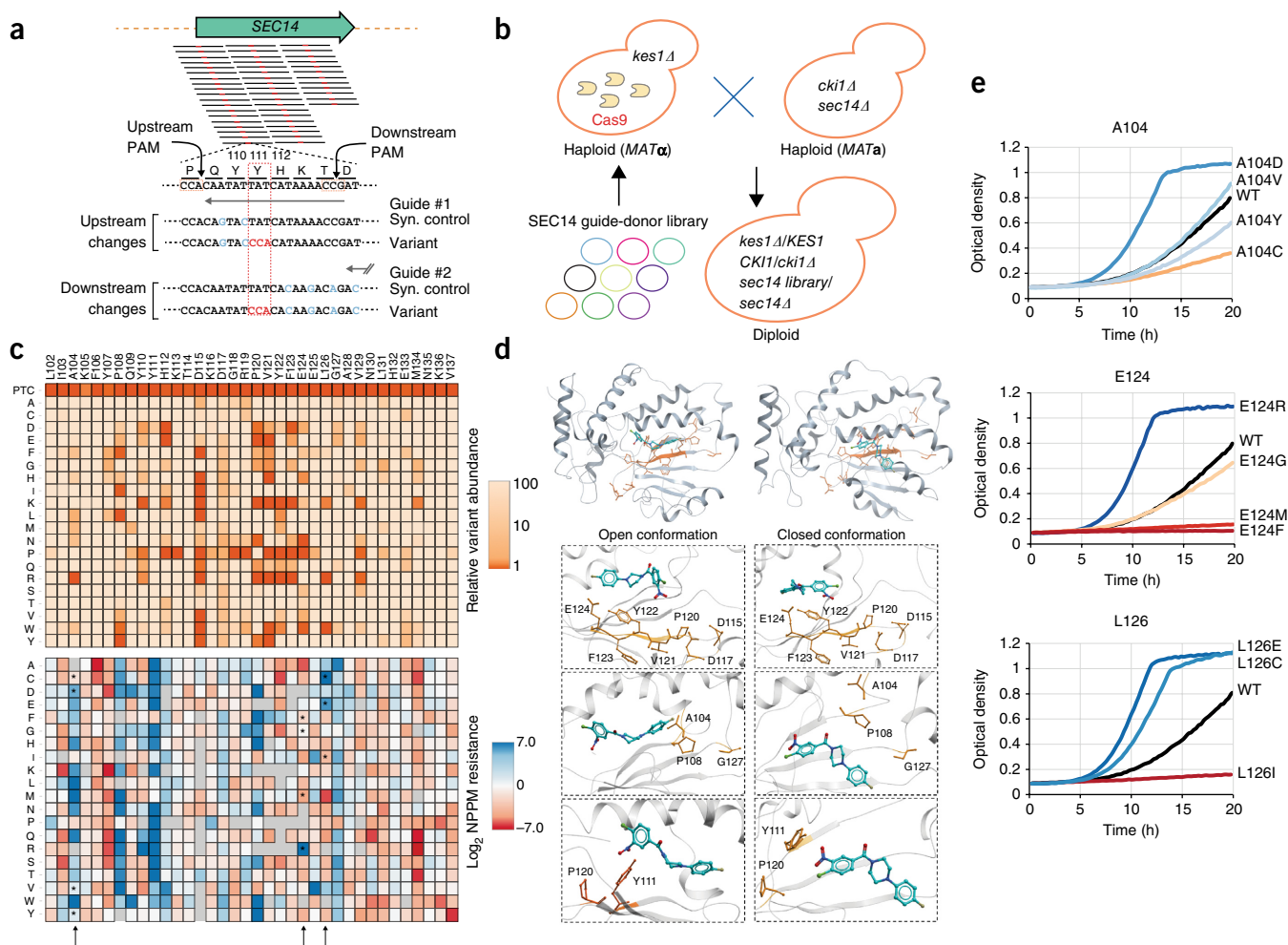
Figure 4 Saturation mutagenesis of an essential eukaryotic gene and structure-function mapping of drug resistance. (**a**) Synonymous-codon-spreading strategy for complete saturation mutagenesis of ORFs (**Supplementary Fig. 3**). (**b**) Suppressor strategy for assaying function of Sec14p mutants. (**c**) Heatmaps depicting the fitness cost of each mutation in *SEC14* on protein function (top) and resistance to the Sec14 small-molecule inhibitor NPPM (bottom). The normalized relative abundance of each variant in the diploid library was assessed by sequencing (top), and read counts following ~12 generations of growth in 8 μM NPPM versus DMSO control were used to calculate relative resistance (bottom). Rows indicate specific amino acid substitutions, and columns indicate amino acid position in Sec14. Color intensity indicates the degree to which each amino acid mutation negatively impacted Sec14 function (orange, top panel), and increased (blue) or decreased (red) Sec14 resistance to NPPM (bottom panel). The light gray blocks indicate variants with insufficient read counts. The screen was conducted in biological replicates. (**d**) The Sec14 α-carbon backbone (gray) and the mutated window (orange), with the NPPM modeled into both the open (left) and closed (right) conformers of Sec14. Side chains critical for protein function (top panel) and NPPM resistance (middle and bottom panels) are highlighted relative to the predicted binding position for NPPM. (**e**) The indicated mutants were independently reconstructed and grown with 8 μM NPPM. OD600 was followed over 20 h of growth, with WT growth plotted as reference (black line). Growth assays were conducted in biological triplicate, which produced nearly identical results (**Supplementary Table 2**).

site (**Fig. 4d**)[14,18]. These substitutions likely impair Sec14p::NPPM interactions in the trajectory by which the NPPM enters the Sec14p lipid-binding pocket, by modulating conformational changes that accompany NPPM entry into the Sec14p lipid-binding pocket, or by changing the conformation of the binding pocket itself.

High-throughput construction of natural variants

A major challenge in quantitative genetics is identifying how individual genetic variants affect phenotype at genome scale. Engineering variants pertinent to natural populations with MAGESTIC could be used to address this challenge. As a proof of principle, we introduced a subset of variants from the well-studied vineyard isolate RM11 into the common laboratory strain S288c. We designed guide–donor pairs to target 30,410 out of 44,020 SNPs, 1,629 out of 3,548 indels, and 3,566 out of 4,754 linked variants (combinations of variants within 5 bp

of each other), without the use of accompanying PAM mutations or synonymous changes. These 35,605 variants were selected on the basis of whether they disrupted an NGG PAM or were located anywhere in the 20-bp guide recognition sequence (**Fig. 5a**). To analyze the dynamics of individual barcoded strains during editing, we compared pre- and post-editing barcode abundances. This comparison can reveal factors affecting guide efficacy, as cells undergoing Cas9-induced double-strand breaks are at a competitive disadvantage. As a control, we first examined barcodes tagging dead guides (guides containing oligo synthesis errors predicted to abrogate target recognition and cleavage) and observed a median enrichment of about threefold (**Fig. 5b**). Enrichment decreased for mutated and near-perfect guides, defined as having mutations with progressively less impact on cleavage efficiency (**Fig. 5b**). Perfect guides showed median negative fold-changes, consistent with the negative growth effects associated
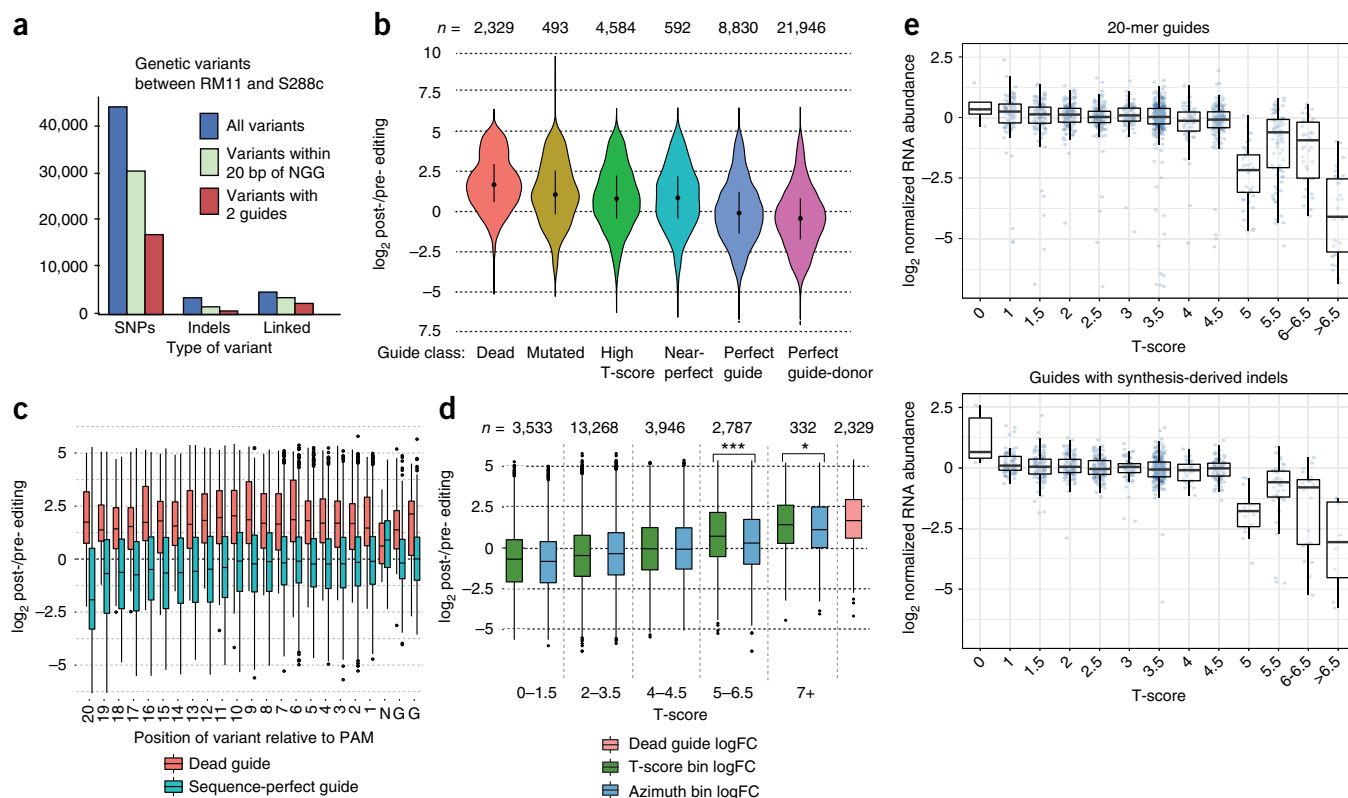
Figure 5 Global profiles of guide efficacy and mismatch tolerance for engineering of natural variants. (**a**) Number of individual genetic variants between RM11 and S288c. (**b**) Log$_2$-fold change (logFC) of barcodes in each guide class post-editing vs. pre-editing (dead guides: indels within 15 bp from PAM or ≥2 mismatches within 18 bp; mutated guides: 1 mismatch within 18 bp or indel from 16–18 bp; near-perfect: mismatches at positions 19 or 20). High T-score is defined as ≥5. (**c**) Dead and perfect guide–donor logFC by distance of the variant allele from the PAM. Variants shown in the N of the NGG consisted solely of indels or linked variants and harbor additional disruption positions upstream or downstream. (**d**) Boxplots of logFC by T-score bin with Azimuth score bins of the same size (one-sided Wilcoxon P-values: *0.03182, ***8.12 × 10^{-14}). (**e**) Normalized RNA abundances as a function of T-score for sequence-perfect guides (top) and guides with synthesis-derived indels (bottom). RNA levels were determined by targeted RT-PCR of the guide RNAs and PCR of the guide DNA sequences followed by high-throughput sequencing. RNA and DNA levels were analyzed in biological triplicates and similar results were obtained with random hexamers and with a structural-guide-specific primer for reverse transcription. Box and violin plots show median value, and 25th and 75th quantiles. The number of barcodes (N) analyzed in each group is shown at the top of each plot for **b** and **d**, and in the Methods, section statistical analysis, for **c**.

with Cas9 cleavage and subsequent DNA repair at that target site. In addition, we reasoned that some guides would be capable of cleaving both their target locus and the donor, leading to multiple cycles of cleavage and repair at the target locus. To this end, we examined how the median enrichment of sequence-perfect guide–donors behaved as a function of variant distance from the PAM.

As expected, dead guides were enriched threefold regardless of variant location. In contrast, cells harboring sequence-perfect guide donors were markedly depleted (**Fig. 5c**). While variants 1 to 10 bp from the PAM showed only mild depletion, variants 11 to 19 bp away exhibited a gradual drop in abundance, with variants at 20 bp from the PAM showing a substantial drop relative to those 19 bp away. This was unexpected, as previous work has suggested that mismatches at the 19th and 20th positions are equally tolerated[19,20]. Overall, our data set analyzing the mismatch tolerance of 23,866 distinct guide–donor pairs across the genome suggests that a substantial fraction of donors with SNPs throughout the guide target region may be competent for editing and subsequent resistance to Cas9-guide cleavage.

An improved guide RNA efficacy scoring system for yeast
Even among sequence-perfect guide–donors, we observed a wide range of log-fold changes (logFCs) in abundance during editing,

suggesting that a subset of sequence-perfect guides are ineffective at target cleavage. To determine whether guides with positive logFCs corresponded to ineffective guides we analyzed the correlation between barcode logFCs and Azimuth efficacy scores, which are widely adopted machine-learning-based scores derived largely from the nucleotide content of the target site and thermodynamics of the guide–target interaction[8]. As expected, we noticed an overall decrease in the distribution of logFC with increasing Azimuth score (**Supplementary Fig. 6a**). We next tested the effect of PAM sequence on efficacy, and noticed a subtle decrease in effectiveness with guides targeting TGG PAMs, consistent with previous results[7] (one-sided Wilcoxon test, $P = 6.48 \times 10^{-5}$; **Supplementary Fig. 6b**).

Many of the highest logFC sequence-perfect guide–donors contained poly-T-stretches, which we reasoned could promote premature termination of Pol III transcription[21,22]. We examined each homopolymer by length, observing that T-homopolymers of lengths 3, 4, and 5 were disfavored more than their A, C, and G counterparts (**Supplementary Fig. 7a**). Furthermore, we noticed that T_3 and T_4 resulted in lower efficacy when located at the 3′-end of the guide (**Supplementary Fig. 7b**). This is likely a consequence of the GTTT sequence in the structural guide component immediately downstream, thus resulting in an extended, imperfect T-stretch. To test whether

these imperfect T-stretches can be used to predict guide efficacy, we assigned each guide a score based on the length of the longest imperfect T-stretch, with penalties for interruptions known to reduce Pol III termination[23] (high T-score defined as ≥5). Notably, the T-score alone predicted guide efficacy to a similar extent as Azimuth (Spearman *rho* −0.18, Pearson $R = -0.19$, both $P < 2.2 \times 10^{-16}$ for Azimuth; $rho = 0.2$, $R = 0.22$, both $P < 2.2 \times 10^{-16}$ for T-score). The T-score remained a significant predictor even after accounting for the guide efficacy variance explained by the Azimuth score (ANOVA test on Azimuth and T-score term, both $P < 2 \times 10^{-16}$, **Supplementary Table 3**). The additional variance explained by the T-score most likely concerns very inefficient guides (T-score ≥ 5, **Fig. 5d** and **Supplementary Fig. 8a**), some of which were predicted to be relatively efficient by Azimuth but showed a logFC > 0 in our data set. This discrepancy is likely due to Azimuth being trained only on single-nucleotide, dinucleotide, and position-independent-nucleotide content[8], none of which would capture imperfect T-stretches.

To confirm that T-scores ≥5 are indicative of reduced guide efficacy because of premature Pol III termination, we analyzed RNA levels globally through reverse transcription and targeted sequencing of the hepatitis delta virus (HDV) ribozyme-guide-structural RNA transcripts. We normalized guide RNA counts to guide DNA counts and binned by T-score. These results revealed decreasing median guide abundance with increasing T-score, with a significant drop from T-score 4.5 to 5—the threshold we had defined for high T-scores (**Fig. 5e**). These results were independent of synthesis-derived errors in the guide, indicating that low RNA levels of high-T score guides are not simply artifacts due to low guide activity (**Fig. 5e**). As we omitted uninterrupted stretches of six or more T's from our guide designs, all T-scores >5 represent imperfect T-stretches. This suggests that T_5-stretches are more potent terminators than imperfect stretches with T-scores of 5.5 or 6.

Relative to yeast Pol III, mammalian Pol III terminates with shorter T-stretches, including T_4 as well as imperfect stretches such $T_2VT_3^{21,23}$. We observed that very few guides in the training set used for the Azimuth algorithm had T-scores ≥5 (**Supplementary Fig. 8b**), which could explain why imperfect T-stretches were not factored in as a predictor. We conclude that incorporation of imperfect T-stretches into machine-learning-based models will lead to improved efficacy predictions and superior guide design algorithms for Pol III-driven guides in yeast and likely in higher eukaryotes as well.

Barcodes serve as accurate proxies for edits

To test how well our barcodes reflect their encoded variants, we sequenced the barcodes of 36 clones isolated after editing. We found that 21 contained guide mutations, consistent with the global enrichment of non-functional guides (**Fig. 5b**), and, as expected, yielded no edits at the target locus. For the remaining 15, we sequenced the target locus and found 9 WT and 6 donor edits (**Supplementary Table 4**). Of these 15 clones, 5 exhibited high T-scores ≥5, all of which were WT at the target locus. We therefore estimate an editing efficiency of 6/10 after excluding 5 high T-score guides and 21 mutated guides. We note that due to the enrichment for non-functional guides, the culture size and sequencing depth needed to assay the edited population effectively increase about fivefold. It is therefore important that the post-editing yeast libraries are not subjected to passage bottlenecks that would result in the loss of low-abundance variants. Overall, this work highlights the power of MAGESTIC to rapidly construct thousands of individual genetic variants, constituting a system for rapidly dissecting quantitative traits down to the nucleotide level by short-barcode sequencing-based counts.

DISCUSSION

Dissecting complex genotype-phenotype relationships has remained a central obstacle in quantitative genetics despite major technological advances in sequencing and genome editing. Assessing the functional impact of genetic variants will be greatly accelerated by robust technologies that can precisely engineer and quantitatively phenotype variants on a large scale. In this study, we develop the MAGESTIC platform to engineer single-nucleotide and amino acid variants genome-wide and quantify fitness by short barcode sequencing.

MAGESTIC surpasses several limitations of currently available methods, namely the instability of plasmid barcodes and the inability to distinguish between oligo synthesis errors and PCR or sequencing errors in the guide and donor during phenotyping[1–3]. First, MAGESTIC separates the steps of guide–donor sequence validation from variant quantification by tagging each guide–donor with a unique short (31-mer) barcode during cloning. A single high-throughput sequencing run with 150-bp paired-end reads can associate each unique barcode with a specific guide–donor sequence at the plasmid library stage. Economical, high-throughput phenotyping can then be achieved with 31-bp reads to count each variant without having to sequence the entire guide–donor for each count. In addition, these barcodes can be used to distinguish cells carrying the same guide–donor pair but deriving from independent editing events, providing internal replicates and serving as single-cell tracers. Second, MAGESTIC efficiently integrates the plasmid barcode into the genome and removes residual guide–donor plasmid via plasmid self-destruction. Integration of the barcode offers several advantages: (1) phenotyping is not confined to environments requiring marker selection, (2) each cell harbors only a single barcode rather than a variable copy number plasmid, and (3) thousands of individual strains can be readily isolated and identified *en masse* from a mutant pool using recombinase-directed indexing[24]. This allows downstream validation of individual variants as well as spatially separated phenotyping, such as measuring productive capacity for bioengineering or protein localization in high-throughput microscopy.

While a previously published guide–donor method developed in prokaryotes (CREATE) employed a one-step cloning procedure by including the guide RNA promoter between the donor and guide sequence[1], this method is not amenable to eukaryotic systems as no eukaryotic promoters are short enough to be included given the current length limitations of array-based oligonucleotide synthesis. A second cloning step is required to either insert the guide RNA promoter, or the structural guide component, with the downside of potentially introducing bias into the library. By maintaining very high coverage at the first step of cloning (a mean of >20 barcodes per variant), we demonstrate that we can maintain complexity and uniform representation of variants in the library (**Supplementary Fig. 1**). In addition, we and others have found that selectable markers in the inserts for the second cloning step remove undesirable background[2].

One of the central challenges in precision genome engineering is creating desired changes with high fidelity and efficiency while avoiding competing pathways of NHEJ-indels and cell death. To address this challenge, we developed a method to actively recruit the donor DNA to the site of DNA breaks using a hybrid LexA–Fkh1p fusion system, and demonstrated a more than fivefold increase in homologous recombination efficiency. Active donor recruitment prevents cells with non-functional guides from overtaking those with functional guides, enabling improved representation of engineered genetic variants in library-scale editing. Although others have shown that tethering donor DNA to Cas9 promotes increased homologous

recombination[25–27], these approaches are not amenable to high-throughput screening as the guide RNA and donor DNA must be expressed separately before physically associating with Cas9. Recruitment of donor DNA to Cas9 breaks by the Fkh1p-phosphothreonine-mediated mechanism offers additional advantages over direct tethering to Cas9, as multiple copies of the donor can be recruited to the break, and enhanced repair does not depend on persistence of Cas9 association with the break. As FHA-recruitment to dsDNA breaks is conserved from yeast to humans[28], it is likely that this mechanism can be adapted to improve editing in NHEJ-prone mammalian systems. A previously published guide–donor method developed in prokaryotes (CREATE) demonstrated significant toxicity due to editing resulting in ~5% survival[1], which is on the order of the ~10% survival we show for yeast in the absence of the Fkh1p–LexA fusion system (**Fig. 3b**). Active donor recruitment should therefore improve library-scale editing approaches in bacterial systems as well.

A major challenge for engineering SNPs is the high-degree of sequence similarity between the guide and the donor, as recognition and cleavage of the donor DNA will result in loss of the variant through cell death or mutation by NHEJ. A second challenge is the availability of PAMs near the SNP, as successful incorporation of the SNP by homologous recombination decreases with increasing distance from the cut site. In this study, we use WT Cas9 and thousands of guide RNAs across the genome, and find that SNPs can be tolerated to differing extents along the guide region, with a significant drop from the 19th to 20th bp positions from the PAM. Ultimately, engineered variants of Cas9 exhibiting reduced mismatch tolerance but maintaining high on-target activity will aid in successful engineering of SNPs throughout the guide region[29–32]. Lastly, we demonstrate that Pol III-terminating T-stretches play a substantial role in dictating guide efficacy in yeast. The use of different promoters, such as Pol II promoters with ribozymes to release the guide from the 5′-cap and poly(A) elements, may address this inherent limitation of delivering guides from the Pol III promoter to T-rich genomic targets. Furthermore, accommodating RNA-guided nucleases with different PAM preferences will broaden the target space of the MAGESTIC system, while specific targeting of highly repetitive regions will remain a challenge with all RNA-guided nuclease approaches. Overall, MAGESTIC enables tens of thousands of specific genetic variants across the genome to be created in a manner that is compatible with robust phenotyping across hundreds of conditions, and will considerably advance our understanding of the genotype–environment–phenotype relationship.

METHODS

Methods, including statements of data availability and any associated accession codes and references, are available in the online version of the paper.

Note: Any Supplementary Information and Source Data files are available in the online version of the paper.

AUTHOR CONTRIBUTIONS
K.R.R., J.D.S., S.C.V., R.P.S., and L.M.S. conceived and designed the study, and wrote and edited the paper. K.R.R., J.D.S., S.C.V., and R.P.S. performed experiments and analyzed data. K.R.R., S.C.V., G.L., and A.R.L. analyzed NGS data; C.S.T., A.C., S.S., M.N., J.H., W.T.B., M.A.M., J.S., and K.M.O. performed experiments. A.T. and V.A.B. performed computational structural analysis on Sec14p-NPPM; W.W. performed variant calling for the different yeast strains. J.E.H. suggested adapting the LexA–Fkh1p system to the guide–donor plasmid. R.S.A., R.W.D., and M.L.S. advised the study. R.P.S. and L.M.S. were responsible for the coordination of the study. All authors read, corrected, and approved the final manuscript.

1. Garst, A.D. *et al.* Genome-wide mapping of mutations at single-nucleotide resolution for protein, metabolic and genome engineering. *Nat. Biotechnol.* **35**, 48–55 (2017).
2. Sadhu, M.J. *et al.* Highly parallel genome variant engineering with CRISPR/Cas9 in eukaryotic cells. Preprint at https://www.biorxiv.org/search/147637 (2017).
3. Guo, X. *et al.* High-throughput creation and functional profiling of eukaryotic DNA sequence variant libraries using CRISPR/Cas9. Preprint at https://www.biorxiv.org/search/195776 (2017).
4. Michlits, G. *et al.* CRISPR-UMI: single-cell lineage tracing of pooled CRISPR-Cas9 screens. *Nat. Methods* **14**, 1191–1197 (2017).
5. DiCarlo, J.E. *et al.* Genome engineering in *Saccharomyces cerevisiae* using CRISPR-Cas systems. *Nucleic Acids Res.* **41**, 4336–4343 (2013).
6. Ugolini, S. & Bruschi, C.V. The red/white colony color assay in the yeast *Saccharomyces cerevisiae*: epistatic growth advantage of white ade8-18, ade2 cells over red ade2 cells. *Curr. Genet.* **30**, 485–492 (1996).
7. Doench, J.G. *et al.* Rational design of highly active sgRNAs for CRISPR-Cas9-mediated gene inactivation. *Nat. Biotechnol.* **32**, 1262–1267 (2014).
8. Doench, J.G. *et al.* Optimized sgRNA design to maximize activity and minimize off-target effects of CRISPR-Cas9. *Nat. Biotechnol.* **34**, 184–191 (2016).
9. Clikeman, J.A., Khalsa, G.J., Barton, S.L. & Nickoloff, J.A. Homologous recombinational repair of double-strand breaks in yeast is enhanced by MAT heterozygosity through yKU-dependent and -independent mechanisms. *Genetics* **157**, 579–589 (2001).
10. Wu, X. & Haber, J.E.A. A 700 bp cis-acting region controls mating-type dependent recombination along the entire left arm of yeast chromosome III. *Cell* **87**, 277–285 (1996).
11. Sun, K., Coïc, E., Zhou, Z., Durrens, P. & Haber, J.E. Saccharomyces forkhead protein Fkh1 regulates donor preference during mating-type switching through the recombination enhancer. *Genes Dev.* **16**, 2085–2096 (2002).
12. Dummer, A.M. *et al.* Binding of the Fkh1 Forkhead Associated Domain to a phosphopeptide within the Mph1 DNA helicase regulates mating-type switching in budding yeast. *PLOS Genet.* **12**, e1006094 (2016).
13. Li, J. *et al.* Regulation of budding yeast mating-type switching donor preference by the FHA domain of Fkh1. *PLoS Genet.* **8**, e1002630 (2012).
14. Chayakulkeeree, M. *et al.* SEC14 is a specific requirement for secretion of phospholipase B1 and pathogenicity of Cryptococcus neoformans. *Mol. Microbiol.* **80**, 1088–1101 (2011).
15. Nile, A.H. *et al.* PITPs as targets for selectively interfering with phosphoinositide signaling in cells. *Nat. Chem. Biol.* **10**, 76–84 (2014).
16. Fang, M. *et al.* Kes1p shares homology with human oxysterol binding protein and participates in a novel regulatory pathway for yeast Golgi-derived transport vesicle biogenesis. *EMBO J.* **15**, 6447–6459 (1996).
17. Li, X. *et al.* Analysis of oxysterol binding protein homologue Kes1p function in regulation of Sec14p-dependent protein transport from the yeast Golgi complex. *J. Cell Biol.* **157**, 63–77 (2002).
18. Cleves, A.E. *et al.* Mutations in the CDP-choline pathway for phospholipid biosynthesis bypass the requirement for an essential phospholipid transfer protein. *Cell* **64**, 789–800 (1991).
19. Fu, B.X.H., St Onge, R.P., Fire, A.Z. & Smith, J.D. Distinct patterns of Cas9 mismatch tolerance in vitro and in vivo. *Nucleic Acids Res.* **44**, 5365–5377 (2016).
20. Hsu, P.D. *et al.* DNA targeting specificity of RNA-guided Cas9 nucleases. *Nat. Biotechnol.* **31**, 827–832 (2013).

21. Arimbasseri, A.G., Rijal, K. & Maraia, R.J. Transcription termination by the eukaryotic RNA polymerase III. *Biochim. Biophys. Acta* **1829**, 318–330 (2013).
22. Braglia, P., Percudani, R. & Dieci, G. Sequence context effects on oligo(dT) termination signal recognition by *Saccharomyces cerevisiae* RNA polymerase III. *J. Biol. Chem.* **280**, 19551–19562 (2005).
23. Orioli, A. *et al.* Widespread occurrence of non-canonical transcription termination by human RNA polymerase III. *Nucleic Acids Res.* **39**, 5499–5512 (2011).
24. Smith, J.D. *et al.* A method for high-throughput production of sequence-verified DNA libraries and strain collections. *Mol. Syst. Biol.* **13**, 913 (2017).
25. Savic, N. *et al.* Covalent linkage of the DNA repair template to the CRISPR/Cas9 complex enhances homology-directed repair. Preprint at https://www.biorxiv.org/search/218149 (2017).
26. Ma, M. *et al.* Efficient generation of mice carrying homozygous double-floxp alleles using the Cas9-Avidin/Biotin-donor DNA system. *Cell Res.* **27**, 578–581 (2017).
27. Gu, B., Posfai, E. & Rossant, J. Efficient generation of targeted large insertions in mouse embryos using 2C-HR-CRISPR. Preprint at https://www.biorxiv.org/search/204339 (2017).
28. Polo, S.E. & Jackson, S.P. Dynamics of DNA damage response proteins at DNA breaks: a focus on protein modifications. *Genes Dev.* **25**, 409–433 (2011).
29. Chen, J.S. *et al.* Enhanced proofreading governs CRISPR-Cas9 targeting accuracy. *Nature* **550**, 407–410 (2017).
30. Kleinstiver, B.P. *et al.* High-fidelity CRISPR-Cas9 nucleases with no detectable genome-wide off-target effects. *Nature* **529**, 490–495 (2016).
31. Slaymaker, I.M. *et al.* Rationally engineered Cas9 nucleases with improved specificity. *Science* **351**, 84–88 (2016).
32. Hu, J.H. *et al.* Evolved Cas9 variants with broad PAM compatibility and high DNA specificity. *Nature* **556**, 57–63 (2018).

ONLINE METHODS

Yeast strains and media. The yeast strain background used in all experiments is a derivative of BY (S288c) named DHY214 (*MATα his3Δ1 leu2Δ0 ura3Δ0 lys2Δ0*) in which genetic defects have been repaired to improve sporulation [*MKT1(30G) RME1(INS-308A) TAO3(1493Q)*] and mitochondrial genome stability [*CAT5(91M) MIP1(661T) SAL1+HAP1+*]. To generate the landing pad at the chromosomal barcode locus, this strain was first transformed with pKR76 (P*TEF1*-Cas9 with *URA3* and *hphMX* markers; https://benchling.com/s/pregddyA) to yield yKR15. yKR15 was then transformed with V79 (*FCY1* guide driven by the tRNA(Tyr)-HDV ribozyme promoter[33]; https://benchling.com/s/1M0BfuaJ) and a linear donor constructed by annealing and extended overlapping oligonucleotides oKR86-oKR87, which introduced a precise deletion in the *FCY1* ORF. A control experiment with an irrelevant donor targeting *CAN1* yielded no surviving colonies, confirming dependence of cell survival on homologous recombination via donor DNA. All eight clones examined exhibited the correct deletion of *FCY1* as confirmed by PCR of the locus and by growth on 5-fluoro-cytosine (5-FC). One clone was selected and named yKR26. To generate the chromosomal barcode locus, the SCEI-*FCY1*-SCEI landing pad was amplified from yACJ2, along with primers with 50 bp of homology upstream and downstream of the SCEI sites to enable integration of the guide–donor cassettes. The homology sequences were randomly generated using the python 2.7 module *random*, and checked for lack of homology to the yeast genome by BLAST[34]. The downstream integration sequence was followed by the *URA3* promoter and the first half of the *URA3* gene, followed by half of an artificial intron and the lox71 site, yielding yJS4 (https://benchling.com/s/seq-8KWFCuPiwZUbhrPRqxFe). The latter construct was included to render these strains compatible with recombinase-directed indexing (REDI)[24]. Transformation of plasmid libraries was performed with a standard lithium-acetate/PEG/ssDNA procedure[35].

Plasmid design. We designed guide–donor plasmids with the precision editing guide under control of a tRNA(Tyr)-HDV promoter. For the *SEC14* editing we used pKR216 (https://benchling.com/s/seq-eyZHbUi3B7xm2BGy0Lbm), which is a 2 μ-plasmid containing counter-selectable *FCY1*, a site for guide X cleavage (TAGGGATAACAGGGTAATGGtgg, PAM in lowercase), and a tandem array of four LexA-sites as well as upstream and downstream homologies for barcode integration. For the natural variant experiments, we created pKR348 (https://benchling.com/s/seq-jGc3L4hiMsI7PFs3wtcg), a 2 μ-plasmid that contains extended overlaps to the barcoding locus, the LexA–Fkh1p fusion under control of the *ADH1* promoter, a tandem array of four LexA sites, a guide X cleavage site, and 200-bp upstream and 300-bp downstream homologies to the barcoding locus. For the barcoding guide (guide X) we tested three different promoters, *RPR1(TetO)*[24], *SNR52*, and tRNA(Tyr)-HDV. As all three promoters showed similar levels of barcode integration and plasmid destruction (**Supplementary Fig. 1**), *RPR1(TetO)* was chosen to drive guide X on pKR348 to enable the option of TetR-controlled expression. For the natural variant experiments, Cas9 was expressed from pKR291 (https://benchling.com/s/seq-tA9exl8LT94qdspLOF2b), under the control of a galactose-inducible promoter to allow for temporal control of Cas9 expression.

Analysis of editing, barcoding, and plasmid-removal kinetics. For experiments described in **Figure 2a,b**, cells were cultured in 48-well plates in an Infinite plate reader (Tecan) at 30 °C with orbital shaking. OD_{600} was followed by taking measurements every ~15 min. Cultures were maintained in log phase growth by passaging cultures every two doublings, when an aliquot of the culture was additionally transferred to a collection plate at 4 °C (Torrey Pines) for further processing. The subpassage and culture sampling steps were triggered by a pre-defined OD (0.6), not by time elapsed. Liquid transfers were performed automatically using a Freedom EVO liquid handling system (Tecan), which was controlled by custom Pegasus software (Tecan). For the colony count analysis for survival on 5-fluoro-cytosine (5-FC) versus YPD, a strain harboring the RM11 natural variants library was grown in quadruplicate in CSM-URA-HIS+ galactose from OD 0.05 to OD 1.6 for the initial five-generation time point and subpassaged into fresh CSM-URA-HIS+galactose at OD 0.05 for subsequent time points. At the indicated generations, ~1,000 cells were plated and the number of colonies on YPD and 5-FC were manually counted. All editing libraries were maintained in CSM-URA-HIS+ glucose before galactose induction.

Active donor recruitment by LexA–Fkh1p. We cloned LexA–Fkh1p under control of the *ADH1* promoter into pKR76 (https://benchling.com/s/pregddyA), a pRS416-based vector also containing Cas9 under the *TEF1* promoter, to give pKR193 (https://benchling.com/s/WLoXhBjL). pKR76 and pKR193 plasmids were separately transformed into yJS4 and an *nej1* null version of yJS4 (yKR139). We then made two mixes of plasmids. The first mix contained 85% by mass an *ADE2* guide–donor 2 μ-plasmid without LexA sites (pKR184), and 15% a 2 μ-plasmid without a functional guide (pKR185). The second mix contained 85% by mass an *ADE2* guide–donor 2 μ-plasmid with 4 LexA sites (pKR194; https://benchling.com/s/ozgmJR2v), and 15% a 2 μ-plasmid without a functional guide (pKR185; https://benchling.com/s/MJO8mPTq). These mixes were transformed using lithium acetate transformation into the four strains expressing Cas9 with or without Fkh1p. The colonies were allowed to grow for a week and then colony counts were generated by counting sectors of the plate to give relative counts for edited colonies, and then plates were washed and gDNA extracted from the population and sequenced at the *ADE2* locus (**Supplementary Table 1**).

Analysis of editing outcomes at *ADE2* and *SEC14* loci. The edited regions for *ADE2* and *SEC14* were amplified with Illumina adapters and sequenced with MiSeq v2 2 × 150 bp reads. All reads were processed with the following BBtools commands with default settings (sourceforge.net/projects/bbmap/). Reads were trimmed with bbduk (version 37.17), merged with bbmerge (version 37.17), and mapped to reference files containing the WT and designed variant sequences using bbmap (version 37.17). Reads mapping with an insertion or deletion in the guide target or PAM sequence were designated as NHEJ-indel events, while reads mapping imperfectly to designed variant sequences in the region harboring the sequence changes were designated as imperfect donor repair events using custom python scripts (see Code Availability).

Guide-donor library design. For *SEC14* saturation mutagenesis, the guide–donor oligonucleotide sequences encoded mutations to convert each amino acid to the other 19 amino acids as well as a stop codon. The highest frequency codon for each amino acid was used for each target amino acid change. For each amino acid, the nearest upstream and nearest downstream PAMs were located and their corresponding guides selected. For the donor DNA, synonymous codons (selected on the basis of the largest hamming distance relative to the codon, with the exception of suboptimal codons with usage frequencies less than 10%) were introduced between the target amino acid and the Cas9 cut site (3 bp upstream of the PAM), until a disruption score of 6 was achieved for the synonymous-change-only donor control. Disruption scores were calculated by aligning the guide to the donor, with disruptions in the GG of the NGG PAM counting as 3 for each disruption, disruptions in the PAM proximal 10 bp (i.e., "seed" region) as 2 each, and disruptions in the PAM distal 10 bp as 1 each. Disruptions refer to either mismatches or indels in the alignment. The disruption score of 6 was intended to ensure complete lack of guide cleavage activity on the donor DNA. For the natural variant libraries, the guide–donor oligonucleotide sequences were designed by first generating VCF files by comparing bam files from novoalign mapping (version 3.07.00, default settings) of Nextera-prepped whole-genome sequencing samples (75 bp paired-end reads) for RM11-1a and SK1 against DHY214 with SICtools[36]. For each entry in the VCF file, all combinations of variants within 5 bp were included in a "linked" variant category to account for amino acid changes and enable construction of multi-nucleotide variants. Each variant was analyzed on the basis of disrupting either an NGG PAM or the 20 bp upstream of an NGG PAM. Guide RNAs or donor DNAs harboring restriction sites used in the cloning steps (NotI, AscI, or BspQI) were removed from the design. For all libraries, guides were disqualified if they contained the canonical Pol III terminator T_6. The BspQI site with an overhang enabling ligation of the structural guide RNA (GTTTAgaagagc, restriction site recognition sequence in lowercase) was inserted in between the guide and the donor; a forward priming site (GGACTTTggcgcgcc) was appended just upstream of the guide sequence; and 15 bp serving as subpool-specific priming sites were appended to the 3′-end (just downstream of each donor) for each oligo sequence.

Barcoded guide–donor library cloning. Array-synthesized guide–donor oligos were obtained from Twist Biosciences (RM11 library) or Agilent Technologies (SK1 library) at the 170-mer scale. We amplified subpools with a forward primer harboring an AscI restriction site at its 3′-end and a reverse primer with a NotI site at its 5′-end followed by a degenerate barcode encoding a pseudo-random sequence (either NNNVHTGNNNVHTGNNNVHTG NNNVHTGNNN or NNNTGVHNNNTGVHNNNTGVHNNNTGVHNNN) that excludes illegal restriction sites (NotI, AscI, and BspQI), followed by sub-pool-specific priming sequence. The guide–donor oligos were amplified using KAPA HiFi polymerase as directed by the manufacturer in 50 μL total reaction volume with an initial denaturation of 98 °C for 1 min, and then 15 cycles of 98 °C 10s, 60 °C 20s, and 72 °C 30s. Reactions were column-cleaned with the Qiagen QIAquick PCR purification kit. NotI and AscI sites enable sticky-end cloning into a multi-copy recipient vector, with the AscI site at the 3′-end of the guide RNA promoter. 5 μg of each PCR-cleaned reaction was cut with 2 μL of AscI (NEB) and 2 μL of NotI (NEB), 10 μL of 10X CutSmart buffer (NEB), and incubated at 37 °C for 1 h, followed by 20 min of heat inactivation at 80 °C. Reactions were column-cleaned and 400 ng of each insert was ligated with T4 DNA ligase into 1 μg of recipient vector (>7:1 insert:vector) treated with NotI, AscI, as well as CIP (NEB) – either pKR216 (*SEC14* library) or pKR348 (natural variants library) – in a total volume of 20 μL. Ligation reactions were ethanol precipitated by adding 80 μL 100% EtOH and 2 μL of 5M NaOAc pH 5.2 with 1 μL of glycoblue (Ambion), incubated on ice for 10 min and spun at 13.2 k.r.p.m. for 5 min, washed with 70% ethanol, and then resuspended in 3 μL of nuclease-free water (IDT). 1 μL of each reaction was then electroporated into 20 μL NEB 10-beta in 0.1 cm-gap electroporation cuvettes (Bio-Rad) with the Bio-Rad GenePulser electroporator using the settings 1.7 kV, 200 Omega, and 25 μF. Typical time constants ranged from 4.5–4.8 ms. Cells were recovered for 1 h at 37 °C in pre-warmed super optimal broth with catabolite repression (SOC) medium and plated onto pre-warmed LB+Carb plates, with a 1:1,000 dilution to get estimated colony counts. Typical colony counts on this dilution plate ranged from 200 to 2,000. The following day cells were scraped from the plates, and plasmids were extracted with the Qiagen miniprep kit. The guide and donor sequences are separated by a type IIS restriction site (BspQI) that enables cloning with an arbitrary overhang, in this case the GTTT directly 3′ of the guide sequence, to enable cloning in the constant structural component of the guide RNA. 5 μg of the plasmid library was cut with 2 μL of BspQI and 2 μL CIP in a total volume of 100 μL, and column-cleaned. The insert containing the structural guide RNA component with yeast-specific (e.g., *HIS3*) and bacteria-specific (e.g., *kanR*) selection markers was amplified from pKR340 (https://benchling.com/s/seq-7PTZ8FoBXCNwIuXNHSHL) with primers harboring BspQI sequences at their 5′-ends. The reverse primer included an additional barcode (bc*; either NNNNNN or NNNNNNHVVNHBBHBHD) situated 3′ of the Illumina read 2 priming sequence, modified to contain a G-to-A SNP at the first position of the BspQI site. These second-step libraries were ligated and electroporated with the same conditions described above (i.e., same as the first step libraries), except that the bacteria were selected with kanamycin to enable enrichment of vectors harboring the insert.

SEC14 mutagenesis and phenotyping. *SEC14* is an essential gene. To detect mutations that impair *SEC14* function without causing cell death, we took advantage of two known 'Sec14p bypass' suppressors, *CKI1* and *KES1* (Cleves *et al.*[18]). We introduced all *SEC14* genetic modifications in a *MAT***a** *kes1*Δ haploid strain carrying the plasmid pKR197 (https://benchling.com/s/s3Xpa5CQ) expressing Cas9 from the *TEF1* promoter and LexA–Fkh1p from the *ADH1* promoter. We also created a second suppressor strain by deleting the entire *SEC14* open reading frame (ORF) in a *MAT*α *cki1*Δ haploid strain. Following mutagenesis of *SEC14* using our CRISPR–Cas9 editing system, the *MAT***a** sec14 mutant pool was mated *en masse* to the *MAT*α *cki1*Δ *sec14*Δ suppressor strain, by mixing equal numbers of *MAT***a** and *MAT*α cells in 3 ml YPD, and incubating that mixture for 6 h at 30 °C with moderate shaking. Diploids were selected by plating the mated culture on media lacking methionine and lysine. After 2 days of growth at 30 °C, diploid colonies were washed off the plate with water, and aliquots were archived at −80 °C in 25% glycerol. The resulting diploid pools contained strains whose viability were dependent on a single copy of *SEC14* containing a genetic modification introduced by our guide–donor library (i.e., *MAT***a**/α, *sec14*Δ/*SEC14**, *cki1*Δ/*CKI1*, *KES1*/*kes1*Δ).

To phenotype our library of *SEC14* variants, we used competitive growth followed by Illumina sequencing of the edited locus to quantify individual strain fitness. *SEC14* variant pool cultures were inoculated from frozen aliquots to a final concentration of 0.1 OD/ml in 20 ml of YPD medium, and grown for 4 h at 30 °C with moderate shaking. 700 μl aliquots of this culture were then transferred to 48-well plates and grown in the presence of 8 μM of the NPPM 4130-1276, or DMSO as a control. Each condition was represented by duplicate cultures. These 48-well plates were grown in an Infinite plate reader (Tecan) at 30 °C with orbital shaking, which allowed growth of cultures to be continuously monitored by taking OD_{600} measurements every ~15 min. Cultures were maintained in log phase growth by automated passaging, in which 80 μl of culture was transferred to a new well containing 620 μl of media upon reaching a 'trigger' OD of 0.76. Liquid transfers were performed using a Freedom EVO liquid handling system (Tecan), which was controlled by custom Pegasus software (Tecan). After three passages (~12 generations total growth), 600 μl of culture at OD 0.76 was transferred to a collection plate stored at 4 °C (Torrey Pines) for further processing. Genomic DNA was extracted from saved cells using the Yeastar genomic kit, as well as an equivalent number of cells from the edited haploid pool, and the diploid "time zero" pool.

From each of these samples, the edited region of *SEC14* was then amplified by PCR containing adapters for Illumina sequencing (NextSeq). Paired-end reads were quality trimmed by bbduk and then merged by bbmerge. Merged read counts mapping to each allele were enumerated by searching for perfect matches to the designed donors. A pseudocount of 1 was added to the number of reads assigned to each variant in each sample. Variant read counts observed in the diploid "time zero" pool were used to generate the *Relative Variant Abundance* heatmap in **Figure 4c**. To calculate *Log2 NPPM Resistance* for each variant, read counts for each duplicate sample were first averaged, and then a log_2 ratio of the NPPM-treated and NPPM-untreated cultures was calculated [i.e., Log2(# reads +NPPM / # reads −NPPM)]. To center the data, we calculated the average log_2 ratio of 44 synonymous *SEC14* control variants, and subtracted that value (−1.848) from all other log_2 ratios. These numbers were used to generate the *Log2 NPPM Resistance* heatmap in **Figure 4c**. Variants that garnered fewer than ten reads in each of the samples were excluded from this plot. In cases where the same mutation was represented by multiple variant strains (e.g., upstream and downstream synonymous versions), the average *Log2 NPPM Resistance* was used to color the heatmap.

To validate the NPPM resistance results, we generated 11 *SEC14* variants individually in a WT background to confirm the accuracy of our suppressor strategy and retested their resistance to 4130-1276 in pure cultures. These variants (A104D, A104V, A104Y, A104C, E124R, E124G, E124M, E124F, L126E, L126C, and L126I) were selected because they exhibited a range of NPPM-resistance phenotypes (**Fig. 4**). Briefly, the strain DHY214 was transformed with a plasmid expressing both constitutive Cas9 and a guide RNA directed to the *SEC14* locus, in the presence of 11 different double-stranded DNA donors encoding the desired mutation surrounded by 60 bases of homology to *SEC14*. Notably, synonymous changes were not introduced in these variants. Introduction of the desired mutation was confirmed by Sanger sequencing. Multiple independent clones (2–4) for each variant, plus empty vector (EV) controls were cultured to saturation overnight in YPD liquid media, diluted to OD 0.1 the next day, and grown in 100-μl cultures in 96-well plates, either in the absence or presence of 8 μM 4130-1276. Growth in each well was monitored in a GENios plate reader (Tecan) by taking OD600 measurements every ~15 min for the duration of the experiment (~20 h). Data from representative wells are plotted in **Figure 4**. All OD measurements are provided in **Supplementary Table 2**.

Protein preparation, homology modeling and computational docking. *Protein preparation.* The X-ray crystal structure of Sec14p (PDB ID 1AUA)[37] was obtained from PDB repository (www.rcsb.org). The protein models were prepared using the *Protein Preparation Wizard* panel in the Schrödinger suite (2017-4, Schrodinger, LLC, New York, NY, 2017). Complete structure of Sec14p was optimized with the OPLS_2005 forcefield in the Schrödinger suite to relieve all atom and bond strains found after adding all missing side chains and/or atoms. The small-molecule model structure for compound 4130-1276 was prepared and energy minimized in MOE (2016.08; Chem. Comp. Group Inc., Montreal, Canada) and the lowest energy conformation was selected for docking.

Homology modeling. A homology model for the closed conformer of Sec14p was generated using the MOE suite (2016.08; Chem. Comp. Group Inc., Montreal, Canada) based on the templates of the open conformer of Sec14p (PDB ID 1AUA)[37] and the closed conformer of Sfh1p bound to PtdIns (PDB ID 3B7N)[38]. Gate residues in the Sec14p open conformation (I215 – Y247) were removed from that template structure before modeling whereas the corresponding gate residues in the closed conformation in Sfh1p/PtdIns were retained. In addition, residues Ala 84–Gln 111 on the far side of the binding pocket from the gate were removed from the Sfh1p template before modeling since they were structurally divergent from the corresponding Sec14p residues. By default, ten independent intermediate models were generated. These different intermediate homology models were generated as a result of permutation selection of different loop candidates and side chain rotamers. The intermediate model, which scored best according to the Amber99 forcefield, was chosen as the final model and was then subjected to further optimization.

Computational docking. Computational docking was carried out using the genetic algorithm-based ligand docking program GOLD 5.2.1 (ref. 36). GOLD explores ligand conformations fairly exhaustively and also provides limited flexibility to protein side chains. For computational docking, the crystal structure of Sec14p in an open conformation (PDB ID 1AUA) and the homology model in closed conformation was used. The active site was defined by taking residue Ser173 in the crystal structure as a reference center to define the protein binding site of radius 6 Å around it, with the GOLD cavity detection algorithm. GOLD docking was carried out without using any constraints or biases to explore all possible diverse solutions. In order to explore all the possible binding modes, docking was carried out to generate diverse solutions with early termination turned off. All other parameters were as the defaults. Compound 4130-1276 was then docked and scored using CHEMPLP scoring function within GOLD as it has been found to give the highest success rates for both pose prediction and virtual screening experiments against diverse validation test sets. Ligand was docked in independent runs with early termination of ligand docking switched off, and the top three best solutions were retained for each run.

Evaluating library representation. In order to assess changes in library representation from the initial oligo library through the transformation into yeast, coverage of barcodes and designed guide–donor variants (features) was compared across the different stages of SK1 natural variants library construction (**Supplementary Fig. 1**). Guide-donor cassettes were amplified with custom-designed indexed primers containing Illumina read primer sequences and sequenced on Nextseq 550 v2 2 × 150 bp paired-end format (step 1 plasmids), 31 + 45 bp paired-end format (step 2 plasmids) or 31 + 120 bp paired-end format (yeast libraries). For determining variant representation in the initial oligo library, 134 bp of the guide–donor sequence were extracted from the forward reads and mapped to the designed variant library using BLASTn alignment. Alignments with greater than 98% identity for length ≥133 bp were used to determine the number of guide–donor variants represented. To examine step 1 coverage from paired-end reads, barcodes were extracted from the first 31 bp of the forward read; all reads for a given barcode were then collapsed to generate a guide–donor consensus sequence for mapping to the library reference using BLASTn. Reads in subsequent steps were mapped directly to the library reference using step 1 annotations. Guide-donor consensus sequences at step 1 were not generated for barcodes with coverage fewer than ten reads.

Pre- and post-editing dynamics. For the analysis in **Figure 5** and **Supplementary Figures 5–8**, the RM11 natural variants yeast library was recovered from a glycerol stock in SC-URA-HIS glucose medium (6.9 g/l yeast nitrogen base (Formedium), 2% D-glucose (Sigma), 1.92 g/l -URA-HIS dropout mixture (Formedium)) for 2 h, then washed and transferred to SC-URA-HIS galactose medium (2% galactose instead of glucose) for seven generations of editing. For editing, the recovered stock was split into five replicates, each inoculated at $OD_{600} = 0.00327$, corresponding to an ~1,000× coverage of the library. Generations were counted based on OD_{600} at the time of sampling. Genomic DNA was extracted using the MasterPure kit (Epicentre) and custom-designed indexed primers containing Illumina read primer sequences were used to amplify the barcodes. Samples were sequenced with Nextseq 550 v2 31x120 bp paired-end format and barcode counts derived by mapping

the 31-mer barcode read to the step 1 reference table. For analysis of barcode dynamics during editing, barcode counts were filtered to remove barcodes not present in the pre-editing sample and barcodes missing in more than one of the five post-editing samples. We further required a minimum count of 20 for barcodes pre-editing. We used edgeR to obtain normalized counts and determine fold-change for each barcode during editing. For the analysis in **Figure 5c,d** and **Supplementary Figures 6–8** we only included barcodes tagging a dead guide or sequence perfect guide–donors. We further excluded all barcodes tagging sequence perfect guide–donors aligning to other parts of the genome with less than two mismatches. T-score is defined by the length of the longest T-stretch in the guide (with the downstream sequence GTTT) with up to two non-T residues, with penalties of 0.5 for one non-T residue and 2.5 for two non-T residues. A high T-score is defined as ≥5, based on the median log-fold change of these score bins being >0. For **Figure 5d**, original T-scores were re-binned into five bins to group original score bins with similar log fold-change distributions and thereby remove redundancy (Bin 0: 0–1.5, Bin 1: 2–3.5, Bin 2: 4–4.5, Bin 3: 5–6.5, Bin 4: 7.5–9.5). To allow visual comparison between the discrete T-score and the continuous Azimuth score in **Figure 5d**, we also binned the Azimuth score, such that the same number of barcodes was included in each bin as for the T-score. We ordered barcodes according to decreasing Azimuth score and assigned the first n barcodes (where n = number of barcodes in T-score bin 0) to Azimuth bin 0, and so on for the rest of the barcodes. For **Figure 5d** and **Supplementary Figures 6b** and **7b** we used a one-sided Wilcoxon rank-sum test to determine if the difference in location between groups was greater than 0. ANOVA terms and parameters are given in **Supplementary Table 3**.

Barcode to edit correspondence. Genomic DNA of 36 individual colonies was extracted using the MasterPure kit (Epicentre), and the barcode locus was amplified and sent for Sanger sequencing. We matched the 31-mer barcodes to our step 1 reference tables and used the CIGAR strings in the reference tables to mark guides containing a mutation relative to the design (number of perfect matches at beginning of CIGAR < 20). To confirm these guides were indeed mutated we amplified the guide sequences from the barcode locus separately and used BLAST+ (version 2.4.0) to align these traces to the oligo library designs. We also extracted the donor sequences from the Sanger traces and aligned them to the oligo library designs to ensure that only the designed mutations were encoded in the donor. We designed primers for amplifying the target sites using primer 3 (release 2.3.7), such that the forward and reverse primers were located symmetrically around the expected edit and the final product size would be 550–600 bp. We further specified a maximal GC content of 60%, length between 18 and 25 nt, and the presence of at least one G or C at the 5′ and 3′ ends of each primer. The target sites were amplified using the previously extracted genomic DNA and sent for Sanger sequencing. To determine editing outcome we aligned the Sanger traces to the yeast genome (R64-2-1) using BLAST+.

Detailed information summarizing the experimental design, statistical parameters, and materials and reagents can be found in the accompanying Life Sciences Reporting Summary.

All statistical analyses were performed in R[39] using the stats package (version 3.3.3 and 3.5.0), with the numbers tested indicated in the main or supplementary figures. Changes in barcode dynamics were analyzed using the *edgeR* package[40,41] (version 3.16.5). One-sided Wilcoxon rank sum tests for group comparisons were performed using the wilcox.test() function, correlation was estimated using the cor.test() function and the ANOVA analysis used the lm() and anova() functions. Box plot elements show the median (black line) and quantile values (box denotes 25th and 75th quantile), with outliers shown as black dots outside of the box whiskers. Violin plots show median (black dot), 25th and 75th quantile (black line) and distribution of the groups. For **Figure 5c**, the number of barcodes per group is given below. For each PAM distance, the first value corresponds to the number of barcodes tagging dead guides and the second value to number of barcodes tagging perfect-guide–donors. $N_{20} = 101/487$, $N_{19} = 74/562$, $N_{18} = 89/743$, $N_{17} = 101/789$, $N_{16} = 88/747$, $N_{15} = 117/741$, $N_{14} = 125/951$, $N_{13} = 94/823$, $N_{12} = 118/915$, $N_{11} = 119/973$, $N_{10} = 123/1158$, $N_{09} = 118/1274$, $N_{08} = 137/1498$, $N_{07} = 112/1373$, $N_{06} = 125/1855$, $N_{05} = 126/1799$, $N_{04} = 114/1544$, $N_{03} = 116/1572$, $N_{02} = 152/1832$, $N_{01} = 121/1677$, $N_{00} = 4/61$, $N_{-01} = 29/297$, $N_{-02} = 25/330$.

All figures were prepared using Adobe Illustrator CS6. Plots were generated in R using package ggplot2[42] (version 2.2.1) or Python 2.7 or 3.6.3 using matplotlib[43] and seaborn[44] plotting libraries. The heatmaps in **Figure 4** were generated with Spotfire (version 7.6.1). All analyses in **Figure 5** and **Supplementary Figures 5**–**7** and **8** were performed in R[39] (version 3.3.3) and plots were generated using ggplot2[42].

Accessions. Protein Data Bank: 1AUA (open conformer of Sec14p), 3B7N (closed conformer of Sfh1p)

Code Availability. All code used to design guide–donor oligo libraries and analyze sequencing data is available here: https://github.com/k-roy/MAGESTIC.

Life Science Reporting Summary. Further information on experimental design is available in the Nature Research Reporting Summary linked to this article.

Data Availability. All sequencing data associated with this study (**Figs. 2a**, **4c**, and **5b**–**d**) are available from the European Nucleotide Archive (ENA) under primary accession number PRJEB23616.

33. Ryan, O.W. *et al.* Selection of chromosomal DNA libraries using a multiplex CRISPR system. *eLife* **3**, e03703 (2014).

34. Altschul, S.F., Gish, W., Miller, W., Myers, E.W. & Lipman, D.J. Basic local alignment search tool. *J. Mol. Biol.* **215**, 403–410 (1990).
35. Gietz, R.D. & Schiestl, R.H. High-efficiency yeast transformation using the LiAc/SS carrier DNA/PEG method. *Nat. Protoc.* **2**, 31–34 (2007).
36. Xing, X. & Wei, W. *SICtools: Find SNV/Indel differences between two bam files with near relationship*. R package version 1.8.0. (2014). http://bioconductor.org/packages/SICtools/.
37. Sha, B., Phillips, S.E., Bankaitis, V.A. & Luo, M. Crystal structure of the *Saccharomyces cerevisiae* phosphatidylinositol-transfer protein. *Nature* **391**, 506–510 (1998).
38. Jones, G., Willett, P., Glen, R.C., Leach, A.R. & Taylor, R. Development and validation of a genetic algorithm for flexible docking. *J. Mol. Biol.* **267**, 727–748 (1997).
39. R Core Team. *R: A Language and Environment for Statistical Computing* (R Foundation for Statistical Computing, 2018).
40. Robinson, M.D., McCarthy, D.J. & Smyth, G.K. edgeR: a Bioconductor package for differential expression analysis of digital gene expression data. *Bioinformatics* **26**, 139–140 (2010).
41. McCarthy, D.J., Chen, Y. & Smyth, G.K. Differential expression analysis of multifactor RNA-Seq experiments with respect to biological variation. *Nucleic Acids Res.* **40**, 4288–4297 (2012).
42. Wickham,, H. *ggplot2: Elegant Graphics for Data Analysis* (Springer, 2009).
43. Hunter, J.D. Matplotlib: A 2D graphics environment. *Comput. Sci. Eng.* **9**, 90–95 (2007).
44. Waskom, M. *et al. seaborn: v0.7.1 (June 2016)* (Zenodo, 2016). doi:10.5281/zenodo.54844.

nature research

Corresponding author(s): Lars M. Steinmetz and Robert P. St.Onge

☐ Initial submission ☐ Revised version ☒ Final submission

Life Sciences Reporting Summary

Nature Research wishes to improve the reproducibility of the work that we publish. This form is intended for publication with all accepted life science papers and provides structure for consistency and transparency in reporting. Every life science submission will use this form; some list items might not apply to an individual manuscript, but all fields must be completed for clarity.

For further information on the points included in this form, see Reporting Life Sciences Research. For further information on Nature Research policies, including our data availability policy, see Authors & Referees and the Editorial Policy Checklist.

▶ Experimental design

1. Sample size

Describe how sample size was determined.

No statistical methods were used to predetermine sample size. For the ADE2 editing time-course shown in Fig.2, samples were assayed with biological duplicates for sequencing. In addition to the published duplicate data, the experiment was also repeated multiple times with generations from 1-9 and identical kinetics of barcoding and editing were obtained. For the donor recruitment experiment in Fig.3, the experiments were performed in triplicate. In addition to these published triplicate data, the experiment was performed numerous additional times with the same result. For the sequencing experiments shown in Fig. 4, the experiment was performed in duplicate and leveraged the use of internal replicates in that each edit is generated with both upstream and downstream synonymous changes. The agreement between the replicate screens as well as these internal controls was high (Supp. Fig. 4, Pearson $R >= 0.88$). For the pre-editing and post-editing analysis of guide-donor barcode abundance shown in Fig. 5, a single pre-editing sequencing dataset was compared against five post-editing replicates (with good agreement (Pearson $R > 0.99$, Spearman rho > 0.72). The conclusions are based on the performance of $>20,000$ guide RNAs in this experiment. For the experiment in Fig 5e., the yeast library was assayed in biological triplicates for normalized RNA abundance measurements.

2. Data exclusions

Describe any data exclusions.

No data were excluded.

3. Replication

Describe whether the experimental findings were reliably reproduced.

All replication attempts gave identical results.

4. Randomization

Describe how samples/organisms/participants were allocated into experimental groups.

Not relevant to this study as yeast cultures involve on the order of millions of individual cells.

5. Blinding

Describe whether the investigators were blinded to group allocation during data collection and/or analysis.

Blinding not relevant to the present study. However, wherever possible labels for samples during computational or visual analysis were given a systematic numbering (e.g. plates for red/white colony counting) such as to minimize any potential bias.

Note: all studies involving animals and/or human research participants must disclose whether blinding and randomization were used.

6. Statistical parameters

For all figures and tables that use statistical methods, confirm that the following items are present in relevant figure legends (or in the Methods section if additional space is needed).

n/a	Confirmed	
☐	☒	The <u>exact sample size</u> (*n*) for each experimental group/condition, given as a discrete number and unit of measurement (animals, litters, cultures, etc.)
☐	☒	A description of how samples were collected, noting whether measurements were taken from distinct samples or whether the same sample was measured repeatedly
☐	☒	A statement indicating how many times each experiment was replicated
☐	☒	The statistical test(s) used and whether they are one- or two-sided (note: only common tests should be described solely by name; more complex techniques should be described in the Methods section)
☐	☒	A description of any assumptions or corrections, such as an adjustment for multiple comparisons
☐	☒	The test results (e.g. *P* values) given as exact values whenever possible and with confidence intervals noted
☐	☒	A clear description of statistics including <u>central tendency</u> (e.g. median, mean) and <u>variation</u> (e.g. standard deviation, interquartile range)
☐	☒	Clearly defined error bars

See the web collection on statistics for biologists for further resources and guidance.

▶ Software

Policy information about availability of computer code

7. Software

Describe the software used to analyze the data in this study.

Custom code was developed in the Python programming language to design the guide-donor oligonucleotide libraries, to analyze the SAM files from bbmap output in order to determine fraction of NHEJ and donor-editing for Fig. 2a, assign counts to specific amino acid mutants in Fig. 4c, and to assign barcodes to mapped guide-donors and count barcodes in Fig 5. All custom code is summarized in the Methods section and complete scripts are available at: https://github.com/k-roy/MAGESTIC. All statistical analyses were performed in R using the stats package (version 3.3.3 and 3.5.0), with the numbers tested indicated in the main or supplementary figures. Changes in barcode dynamics were analyzed using the edgeR package (version 3.16.5). One sided Wilcoxon rank sum tests for group comparisons were performed using the wilcox.test() function, correlation was estimated using the cor.test() function and the ANOVA analysis used the lm() and anova() functions. All figures were prepared using Adobe Illustrator CS6. Plots were generated in R using package ggplot2 (version 2.2.1) or Python 2.7 or 3.6.3 using matplotlib and seaborn plotting libraries. The heatmaps in Fig. 4 were generated with Spotfire (version 7.6.1).

For manuscripts utilizing custom algorithms or software that are central to the paper but not yet described in the published literature, software must be made available to editors and reviewers upon request. We strongly encourage code deposition in a community repository (e.g. GitHub). *Nature Methods* guidance for providing algorithms and software for publication provides further information on this topic.

▶ Materials and reagents

Policy information about availability of materials

8. Materials availability

Indicate whether there are restrictions on availability of unique materials or if these materials are only available for distribution by a for-profit company.

All yeast strains and materials used in this study are available to the community upon request.

9. Antibodies

Describe the antibodies used and how they were validated for use in the system under study (i.e. assay and species).

No antibodies were used.

10. Eukaryotic cell lines

a. State the source of each eukaryotic cell line used.

The primary cell line used in this study is DHY214, an S288c-based strain developed at the Stanford Genome Technology Center by Angela Chu and Joe Horecka. This strain contains the following genotype (MATα his3Δ1 leu2Δ0 ura3Δ0 lys2Δ0) with repaired sporulation [MKT1(30G) RME1(INS-308A) TAO3(1493Q)] and mitochondrial genome stability [CAT5(91M) MIP1(661T) SAL1+ HAP1+].

b. Describe the method of cell line authentication used.

All repaired alleles in this strain were verified first by PCR of genomic DNA followed by Sanger sequencing. To further verify the strain, we conducted whole genome-sequencing with Nextera tagmentation library prep kit and verified the presence of the designed mutations.

c. Report whether the cell lines were tested for mycoplasma contamination.

Mycoplasma contamination is not a known issue with yeast cultures. When possible, yeast cultures were kept when possible in G418 and HygB-containing media to eliminate any other potential contamination.

d. If any of the cell lines used are listed in the database of commonly misidentified cell lines maintained by ICLAC, provide a scientific rationale for their use.

No commonly misidentified cell lines were used.

▶ Animals and human research participants

Policy information about studies involving animals; when reporting animal research, follow the ARRIVE guidelines

11. Description of research animals

Provide details on animals and/or animal-derived materials used in the study.

No animals were used.

Policy information about studies involving human research participants

12. Description of human research participants

Describe the covariate-relevant population characteristics of the human research participants.

This study did not involve human participants.